IEEE Access
Multidisciplinary ⋮ Rapid Review ⋮ Open Access Journal

Received July 23, 2021, accepted August 2, 2021, date of publication August 5, 2021, date of current version August 11, 2021.

Digital Object Identifier 10.1109/ACCESS.2021.3102628

Disturbance Observer-Based Robust Model Predictive Control for a Voltage Sensorless Grid-Connected Inverter With an LCL Filter

NGUYEN NGOC NAM[1,2], NGOC-DUC NGUYEN[3], CHANGWOO YOON[3], AND YOUNG IL LEE[1], (Senior Member, IEEE)

[1]Department of Electrical and Information Engineering, Seoul National University of Science and Technology (SeoulTech), Seoul 01811, South Korea
[2]Faculty of Electrical and Electronic Engineering, Phenikaa University, Hanoi 12116, Vietnam
[3]Research Center of Electrical and Information Technology, Seoul National University of Science and Technology (SeoulTech), Seoul 01811, South Korea

Corresponding author: Young Il Lee (yilee@seoultech.ac.kr)

This work was supported by the Advanced Research Project through Seoul National University of Science and Technology (SeoulTech) under Grant 2021-0205.

ABSTRACT This paper proposes a disturbance observer-based robust model predictive control (MPC) for a voltage sensorless grid-connected inverter with an inductive-capacitive-inductive (LCL) filter. A full-state estimator and a grid voltage observer are designed to reduce the number of sensors. A lumped disturbance observer, considering the parameter mismatch along with the grid impedance variation, is also designed to eliminate the steady-state error. A cost function, which consists of the error state and control input, is employed in the MPC design. Based on the Lyapunov stability, the full-state observer, voltage estimation, lumped disturbance observer, and the robust controller gains are obtained by solving an optimization problem based on linear matrix inequality (LMI). A frequency response analysis of the entire system is conducted to verify the reference tracking and disturbance rejection outcomes. As a result, the state and grid voltage observer outcomes converge to the actual values as rapidly as possible. The effectiveness of the proposed control method is demonstrated in comparison with the proportional-integral (PI) approach and with a controller recently proposed in the literature. Simulation and experimental results are presented to verify the effectiveness of the proposed method under LCL parameter uncertainties and grid impedance variations.

INDEX TERMS Sensorless model predictive control (MPC), disturbance observer, three-phase inverters, inductive-capacitive-inductive (LCL).

I. INTRODUCTION

Recently, grid-voltage sensorless control has attracted much attention for interfacing renewable energy sources (RESs) to the utility grid [1]–[4], [6]–[14]. The primary purpose of grid voltage measurements is to extract the grid phase angle to synchronize the inverter to the utility grid. However, the conventional grid voltage measurement method incurs a high hardware cost and is relatively complex given the many sensors that are required when using it. To overcome this challenge, grid voltage estimation can be used to determine the grid phase angle. Furthermore, voltage sensorless control can mitigate electrical noise and failures of voltage sensors.

In grid-connected inverter (GCI) applications, the switching harmonics generated by the inverter can be attenuated by an inductor (L), an inductor-capacitor (LC), or an inductor-capacitor-inductor (LCL) filter. Among them, the LCL filter is more widely employed because it can attenuate high-frequency pulse-width-modulation (PWM) switching harmonics and reduce the overall inductor size and hardware cost compared to the L and LC filters [5].

However, an LCL filter's underdamped characteristics, caused by the filter resonant frequency, is an obstacle that prevents the wider practical use of LCL filters. System instability can arise if the controller is improperly designed. Moreover, most of the current control for a GCI is built based on a mathematical model. Thus, the current control performance is affected by the LCL parameter uncertainties and the grid impedance variation.

In several earlier studies [6]–[10], adaptation law is employed to estimate the grid voltage and to extract the grid phase angle. In particular, an adaptive neural network

The associate editor coordinating the review of this manuscript and approving it for publication was Yonghao Gui.

is developed to estimate the grid voltage [6], allowing the magnitude and phase of the fundamental grid voltage to be extracted using an adaptive neural filter. This method guarantees that the grid voltage can be obtained with high accuracy. However, this study used an L filter. Furthermore, in other work [9], a predictive current control is employed, and an adaptive steepest descent method is used to estimate the grid voltage. Another study investigates a frequency-adaptive grid-voltage sensorless control in which the grid voltage and the harmonics components are simultaneously estimated [7]. In particular, the system model is developed in a stationary frame, and its full-state observer is therefore not affected by the frequency [7]. In contrast, other researchers [8], [10] present an observer-based grid-voltage sensorless scheme that simultaneously estimates both positive and negative sequences under an unbalanced grid condition. As a result, a fast-tracking reference is achieved. Another work in [22] presents the MPC of three-phase PWM under the unbalance and distortion conditions. The cascaded delay signal cancellation method is used to obtain the grid voltage. However, the model uncertainties and variations in the grid impedance were not taken into consideration in these studies [6]–[10] and [22].

To deal with the LCL parameter uncertainties and grid impedance variation, several strategies have been proposed [11]–[16]. In particular, the concept of the lumped disturbance, containing the grid voltage and LCL parameter uncertainties, has been obtained based on a neural network [11], [12]. More specifically, the accurate grid voltage is extracted from the lumped disturbance based on the filter. However, this method is proposed for an LC filter as opposed to an LCL filter. Also in the literature is the extended state observer (ESO) [13]–[15] as a promising solution for the voltage sensorless current control of a GCI. In this method, the grid voltage is modeled as an extended state. Specifically, robust current control is utilized for a voltage sensorless GCI system with the grid voltage considered as a disturbance [13], [14]. With the ESO, the full state and grid voltage are estimated. Then, the disturbance observer is updated to the system model to compensate for the actual disturbance. Moreover, the observer and controller gains are obtained by solving the LMI problem for robustness control. As a result, good tracking performance is achieved, and the filter resonant frequency is suppressed. However, the lumped disturbance, which contains the LCL parameter uncertainties and the grid impedance, has not been explicitly considered. However, the lumped disturbance, which contains the mismatch model and grid voltage, has been considered [15]. In this method, the estimated grid voltage is extracted from the lumped disturbance, and a proportional-integral (PI) controller is employed. Although the lumped disturbance, which contains the mismatched model and grid impedance, is estimated, a severe transient response may still arise due to the unknown initial grid phase angle. Similarly, Tran *et al.* [23] proposed an ADRC with resonant extended state observer for a GCI. Moreover, the adaptive grid frequency is also considered in order to deal with the different grid voltage frequency levels.

This paper proposes a disturbance observer-based robust model predictive control for a voltage sensorless GCI with an LCL filter considering the parameter uncertainties and grid impedance variation explicitly. Unlike earlier work in this area [14], the inverter-side inductance levels and grid impedance variations are considered in this paper. It is essential to consider parameter uncertainties during the design of an estimator and controller for an LCL-filtered grid-connected inverter. Significantly, the grid impedance is uncertain, and this factor can change the parameters of an LCL filter.

The cost function, which consists of the state error and the control input, is employed in our scheme to design a robust current control for the GCI system under a mismatch model with grid impedance variation. Furthermore, the full-state variable and the grid voltage are simultaneously estimated to reduce the number of sensors. Grid voltage estimation is used to extract the grid phase angle using a phase-locked loop (PLL) to facilitate synchronization. The initial grid phase angle is detected using the grid-side current sensor, allowing the inverter to be easily synchronized with the grid during the start-up process. A lumped disturbance observer is presented to compensate for the mismatched model and grid impedance variation. Notably, a systematic way to obtain the full-state observer, voltage observer, lumped disturbance, and the robust controller gains is provided by leveraging Lyapunov stability theory. The LMI optimization problem is also applied to achieve rapid convergence rates of the states and grid voltages. Moreover, a robust MPC strategy combined with the lumped disturbance is shown to be capable of fast tracking with zero steady-state error. Simulations and experiments are conducted to validate the efficacy of the proposed control scheme under grid impedance and model parameter uncertainties.

The rest of this paper is organized as follows. In Section II, a mathematical model and the modeling of the uncertainties are presented. Section III describes the full-state observer, grid voltage estimator, and the lumped disturbance observer. The robust MPC is designed in Section IV, and the frequency response analysis is presented in Section V. Simulation and experimental results are shown in Section VI. Finally, Section VII concludes this paper.

II. SYSTEM DESCRIPTION

A. MATHEMATICS MODEL

A three-phase GCI interfaced with the utility grid through an LCL filter along with the proposed control structure is illustrated in Fig. 1. In Fig. 1, L_1 and L_2 represent the filter inductors, whose parasitic resistances are denoted by R_1 and R_2, respectively, and C_f is the filter capacitor. V_{DC} and L_g represent the voltage source and uncertain grid inductance, respectively. In this paper, only the grid-side current and V_{DC} voltage are measured, and the grid-side currents are converted into d-q values of the synchronous reference

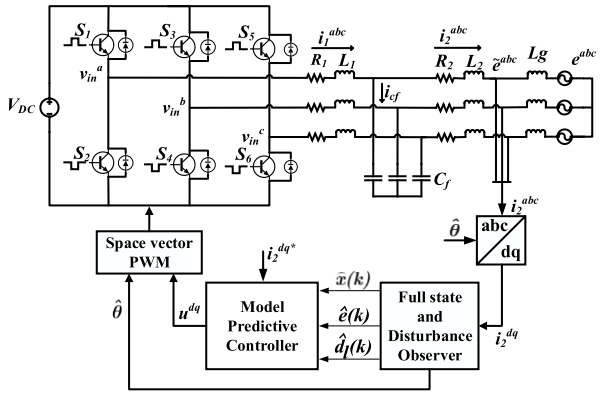

FIGURE 1. The power circuit of a three-phase grid-connected inverter with LCL filters.

frame (SRF). Therefore, the predictive model controller, the full-state observer, the grid voltage estimation, and the robust disturbance observer are designed based on the d-q frame model. Furthermore, voltage estimation is done to extract the grid phase angle for synchronization from the inverter to the grid voltage.

From Fig. 1, the state space equations of the inverter system can be given in SRF as

$$\dot{x}(t) = \phi_c x(t) + \Gamma_c u(t) + H_c e(t) \tag{1}$$
$$y(t) = C_c x(t) \tag{2}$$

where $x = \left[i_2^q\ i_2^d\ i_1^q\ i_1^d\ v_c^q\ v_c^d\right]^T$, $u = \left[v_{in}^q\ v_{in}^d\right]^T$, and $e = \left[e^q\ e^d\right]^T$, with i_2, i_1, v_c, v_{in}, and e being the grid-side current, inverter-side current, capacitor voltage, control input, and the unknown grid voltage, respectively. The control objective is to ensure that the grid-side currents $(i_2^q\ i_2^d)$ approach the desired values $(i_2^{qo}\ i_2^{do})$ as closely as possible in the presence of the parameter and grid impedance uncertainties.

The parametric matrices in (1)-(2) are expressed as follows:

$$\phi_c = \begin{bmatrix} -R_2/L_f & -\omega & 0 & 0 & 1/L_f & 0 \\ \omega & -R_2/L_f & 0 & 0 & 0 & 1/L_f \\ 0 & 0 & -R_1/L_1 & -\omega & -1/L_1 & 0 \\ 0 & 0 & \omega & -R_1/L_1 & 0 & -1/L_1 \\ -1/C_f & 0 & 1/C_f & 0 & 0 & -\omega \\ 0 & -1/C_f & 0 & 1/C_f & \omega & 0 \end{bmatrix},$$

$$\Gamma_c = \begin{bmatrix} 0 & 0 \\ 0 & 0 \\ 1/L_1 & 0 \\ 0 & 1/L_1 \\ 0 & 0 \\ 0 & 0 \end{bmatrix}, \quad H_c = \begin{bmatrix} -1/L_f & 0 \\ 0 & -1/L_f \\ 0 & 0 \\ 0 & 0 \\ 0 & 0 \\ 0 & 0 \end{bmatrix}, \text{ and}$$

$$C_c = \begin{bmatrix} 1 & 0 & 0 & 0 & 0 & 0 \\ 0 & 1 & 0 & 0 & 0 & 0 \end{bmatrix},$$

where ω is an angular frequency of the grid voltage and $L_f = L_2 + L_g$.

For digital implementation, a continuous-time model (1)-(2) is transformed into a discrete-time model with consideration of the input time delay, as follows:

$$x(k+1) = \phi_d x(k) + \Gamma_d u(k-1) + H_d e(k) \tag{3}$$
$$y(k) = C_d x(k) \tag{4}$$

where the matrices Φ_d, Γ_d, C_d and H_d are given as

$$\phi_d = I_{6\times 6} + \phi_c T_s, \quad \Gamma_d = \Gamma_c T_s, \ C_d = C_c, \text{ and } H_d = H_c T_s,$$

respectively, and T_s is the sampling time.

B. MODELING OF UNCERTAINTIES

There are various uncertainties, including the LCL filter parameter uncertainties and the grid impedance variation (3). To reflect these uncertainties, we assume that [17]

$$(L_1)_n/\mu \le L_1 \le (L_1)_n * \mu \tag{5}$$
$$(L_2)_n/\mu \le L_2 \le (L_2)_n * \mu \tag{6}$$
$$(C_f)_n/\mu \le C_f \le (C_f)_n * \mu \tag{7}$$
$$(R_1)_n/\mu \le R_1 \le (R_1)_n * \mu \tag{8}$$
$$(R_2)_n/\mu \le R_2 \le (R_2)_n * \mu \tag{9}$$

where $(\cdot)_n$ indicates the nominal value in each case. The scalar value $\mu(>1)$ is used to define the lower and upper bound for the LCL parameter uncertainties. Moreover, μ is used as a design knob to adjust the performances of the full-state feedback observer, controller, and disturbance observer. In this paper, different values of μ are used for the full-state feedback observer, controller, and disturbance observer. How to obtain the best values of μ will be presented in the section VI.A. This assumption implies that L_1, L_2, C_f, R_1 and R_2 are affected by uncertainties, i.e.,

$$\Pi = \left(\sum_{i=1}^{p} \delta_i \left(\phi_{di}, \Gamma_{di}, H_{di}\right) \middle| \sum_{i=1}^{p} \delta_i = 1, \delta_i > 0 \right) \tag{10}$$

$p = 2^5 = 32$.

The system model (3) can be described in the nominal model and lumped disturbance $d_L(k)$ as follows:

$$x(k+1) = \phi_n x(k) + \Gamma_n u(k-1) + H_n e(k) + d_L(k) \tag{11}$$

where $(\cdot)_n$ denotes a nominal value and $d_L(k)$ is given as

$$d_L(k) = \Delta\phi x(k) + \Delta\Gamma u(k) + \Delta H e(k) \tag{12}$$

with $\Delta\phi = \phi_d - \phi_n$, $\Delta\Gamma = \Gamma_d - \Gamma_n$, and $\Delta H = H_d - H_n$.

III. FULL-STATE ESTIMATION AND DISTURBANCE OBSERVER DESIGN

In the presence of LCL parameter uncertainties, the full-state and grid voltage (FSGV) estimator introduced in earlier work [14] cannot be used. Thus, in this section, a lumped disturbance observer is designed based on an FSGV estimator. This lumped disturbance observer will estimate the effects of LCL parameter uncertainties and grid impedance variations to remove the steady-state FSGV estimation error. First, the design procedure of the FSGV estimator from the aforementioned study [14] is described briefly.

A. FULL-STATE AND GRID VOLTAGE ESTIMATION [14]

It is assumed that the unknown grid voltage in (3) is constant, i.e.,

$$e(k+1) = e(k). \tag{13}$$

Two equations (3) and (13) can be combined in a compact form, as follows:

$$z(k+1) = \phi_z z(k) + \Gamma_z u(k). \tag{14}$$

$$y(z) = \begin{bmatrix} C_d & 0_{2x2} \end{bmatrix} \begin{bmatrix} x(k) \\ e(k) \end{bmatrix} = C_z z(k) \tag{15}$$

where

$$z(k) = \begin{bmatrix} x(k) \\ e(k) \end{bmatrix}, \quad \Phi_z = \begin{bmatrix} \phi_d & H_d \\ 0_{2x6} & I_{2x2} \end{bmatrix},$$
$$\Gamma_z = \begin{bmatrix} \Gamma_d \\ 0_{2x2} \end{bmatrix}, \quad \text{and } C_z = \begin{bmatrix} C_d & 0_{2x2} \end{bmatrix}.$$

The full-state and grid voltage estimations are designed based on the measurement $y(k)$ as

$$\hat{x}(k+1) = \phi_d \hat{x}(k) + \Gamma_d u(k-1) + H_d \hat{e}(k) + L_x \left(y(k) - C_d \hat{x}(k) \right) \tag{16}$$

$$\hat{e}(k+1) = \hat{e}(k) + L_e \left(y(k) - C_d \hat{x}(k) \right) \tag{17}$$

where $\hat{x}(k)$ and $\hat{e}(k)$ represent the estimated state and grid voltage observer, respectively. Furthermore, L_x and L_e are the observer gains. From (16)-(17), an augmented form can be expressed as

$$\hat{z}(k+1) = \phi_z \hat{z}(k) + \Gamma_z u(k-1) + L_z \left(y_z(k) - C_z \hat{z}(k) \right) \tag{18}$$

where $\hat{z}(k) = \begin{bmatrix} \hat{x}(k) & \hat{e}(k) \end{bmatrix}^T$ and $L_z = \begin{bmatrix} L_x & L_e \end{bmatrix}^T$.

To obtain the observer gain L_z, an error dynamic $e_z(k) = z(k) - \hat{z}(k)$ is formed by subtracting (18) from (14); i.e.,

$$e_z(k+1) = (\phi_z - L_z C_z) e_z(k) \tag{19}$$

To ensure the asymptotic stability in (19), L_z must be selected such that $(\phi_z - L_z C_z)$ is a Hurwitz matrix. This condition guarantees that all the eigenvalues of (19) lie inside the unit circle. An objective function is then selected with the positive definite matrix W as

$$V(k) = e_z(k+1)^T W e_z(k+1). \tag{20}$$

The task now is to determine the weighting matrix W and the observer gain L_z so that the object function $V(k)$ monotonically decreases i.e., $(V(k) - V(k-1) < 0)$.

$$V(k) - V(k-1) = e_z(k)^T \left((\Phi_z - L_z C_z)^T W (\Phi_z - L_z C_z) - W \right) e_z(k) < 0 \tag{21}$$

Inequality (21) is ensured if

$$W - (\Phi_z - L_z C_z)^T W (\Phi_z - L_z C_z) > 0. \tag{22}$$

The convergence rate $\rho (0 \leq \rho < 1)$ can be inserted into (22) as:

$$W - (\Phi_z - L_z C_z)^T W (\Phi_z - L_z C_z) > \rho^2 W. \tag{23}$$

From (23) indicates that the maximum convergence rate ρ will make the largest gap in (22). Obviously, (23) is guaranteed if there exist $0 < W_0 < \left(1 - \rho^2\right) W$. As a result, we have

$$W_0 - (\Phi_z - L_z C_z)^T W (\Phi_z - L_z C_z) > 0. \tag{24}$$

By applying the Schur complement, (24) can be rewritten as

$$\begin{bmatrix} W_0 & (W\Phi_z - Y_L C_z)^T \\ (W\Phi_z - Y_L C_z) & W \end{bmatrix} > 0. \tag{25}$$

where $Y_L = W L_z$. Because (Φ_d, H_d) belongs to uncertainties set (10), it is guaranteed that (25) will satisfy for all $(\Phi_d, H_d) \in \Pi$ by the following LMIs:

$$\begin{bmatrix} W_0 & \left(W\phi_{zi} - Y_L C_z\right)^T \\ \left(W\phi_{zi} - Y_L C_z\right) & W \end{bmatrix} > 0, \quad i = 1, 2 \ldots, 32 \tag{26}$$

By replacing $\alpha = 1 - \rho^2$, the matrices W and Y_L can be calculated by minimizing α in the following optimization problem.

$$\begin{aligned} &\min \alpha \; subject \; to \; (26) \\ &W_0 > 0 \\ &W_0 < \alpha W \end{aligned} \tag{27}$$

Then, the optimal observer gain is computed as $L_z = W^{-1} Y_L$.

As soon as the grid voltage estimation is completed, the grid voltage estimation $\hat{e}^q(k)$ is used to extract the grid phase angle using the PLL as shown in Fig.2.

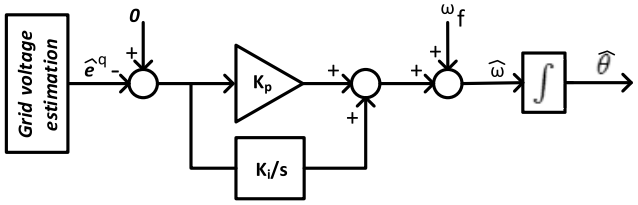

FIGURE 2. Block diagram of the PLL scheme.

B. LUMPED DISTURBANCE OBSERVER DESIGN

The FSGV estimator (16) cannot be implemented in the presence of parameter uncertainties. FSGV estimator should be rewritten using the nominal model and lumped disturbance as follows:

$$\hat{x}(k+1) = \phi_n \hat{x}(k) + \Gamma_n u(k-1) + H_n \hat{e}(k) + L_x \left(y(k) - C_d \hat{x}(k) \right) + \hat{d}_L(k). \tag{28}$$

Note that lumped disturbance estimation $\hat{d}_L(k)$ was used instead of $d_L(k)$ in (28). A lumped disturbance observer can be designed with the observer gain L_d as follows [16]:

$$\hat{d}_L(k+1) = \hat{d}_L(k) + L_d\left(d_L(k) - \hat{d}_L(k)\right). \quad (29)$$

From (11), the expression for the lumped disturbance can be rewritten as

$$d_L(k) = x(k+1) - \phi_n x(k) - \Gamma_n u(k-1) - H_n e(k). \quad (30)$$

Substituting $d_L(k)$ from (30) into (29), we have

$$\hat{d}_L(k+1) = \hat{d}_L(k) + L_d(x(k+1) - \phi_n x(k) - \Gamma_n u(k-1) - H_n e(k) - \hat{d}_L(k)). \quad (31)$$

To determine the lumped disturbance observer, the state $x(k)$ and grid voltage $e(k)$ in (31) are at this point replaced by the $\hat{x}(k)$ and $\hat{e}(k)$, respectively, as estimated in the previous section. Then, (31) can be rewritten as

$$\hat{d}_L(k+1) = \hat{d}_L(k) + L_d(\hat{x}(k+1) - \phi_n \hat{x}(k) - \Gamma_n u(k-1) - H_n \hat{e}(k) - \hat{d}_L(k)). \quad (32)$$

At this stage, we provide a systematic way to obtain the observer gain L_d. The models (3) and (11) can be rewritten in steady-state values as follows.

$$x^o = \phi_d x^o + \Gamma_d u^0 + H_d e^o \quad (33)$$

and

$$x^o = \phi_n x^o + \Gamma_n u^0 + H_n \hat{e}(k) + d_L^o, \quad (34)$$

respectively, where $x^o = \left[i_2^{qo}\ i_2^{do}\ i_1^{qo}\ i_1^{do}\ v_c^{qo}\ v_c^{do}\right]^T$ and $u^0 = \left[u^{q0}\ u^{d0}\right]^T$. Subtracting (34) from (33) yields:

$$\Delta\phi x^o + \Delta\Gamma u^o + \Delta H e^o - d_L^o = 0. \quad (35)$$

By inserting (3) and (35) into (31), the lumped disturbance observer can be written as

$$\hat{d}_L(k+1) = \hat{d}_L(k) + L_d(\Delta\phi\tilde{e}_x(k) + \Delta\Gamma\delta u(k) - (\hat{d}_L(k) - d_L^o)) + L_d\Delta H\delta e^o. \quad (36)$$

$u(k)$ will be determined via $u(k) = u^0 + K\delta\tilde{e}_x(k), \delta u(k) = u(k) - u^0$, where u^0 is the steady-state input to maintain the desired reference states i_2^{qo} and i_2^{do} and K is the optimal feedback gain of the MPC. The method used to obtain u^0 and K will be described in the next section.

Assuming that grid voltage estimation converges well to the actual value, a dynamic state error is then defined by subtracting (33) from (3), as follows:

$$\tilde{e}_x(k+1) = x(k+1) - x^o = (\phi_d + \Gamma_d K)\tilde{e}_x(k) \quad (37)$$

We now define $\tilde{d}_L(k) = \hat{d}_L(k) - d_L^o$; subtracting d_L^o from both sides of (36) will yield

$$\tilde{d}_L(k+1) = (I - L_d)\tilde{d}_L(k) + L_d(\Delta\phi + \Delta\Gamma K)\tilde{e}_x(k) + L_d\Delta H\delta e^o. \quad (38)$$

These two error equations (37) and (38) can be combined to yield

$$\begin{bmatrix}\tilde{d}_L(k+1)\\ \tilde{e}_x(k+1)\end{bmatrix} = \begin{bmatrix} I - L_d & L_d(\Delta\phi + \Delta\Gamma K)\\ 0 & \phi_d + \Gamma_d K\end{bmatrix}\begin{bmatrix}\tilde{d}_L(k)\\ \tilde{e}_x(k)\end{bmatrix} + \begin{bmatrix} L_d\Delta H\\ 0\end{bmatrix}\delta e^o \quad (39)$$

We define a new variable $e_d(k) = \left[\tilde{d}_L(k)\ \ \tilde{e}_x(k)\right]^T$ for (39) to check the stability of its homogeneous response.

$$e_d(k+1) = \psi e_d(k) \quad (40)$$

where

$$\psi = \begin{bmatrix} I - L_d & L_d(\Delta\phi + \Delta\Gamma K)\\ 0 & \phi_d + \Gamma_d K\end{bmatrix}.$$

By following an approach similar to that in (19)-(26), the stability condition for the dynamic error in (40) can be expressed as follows:

$$\begin{bmatrix} M_o & \\ \begin{bmatrix} M_1 - Y_d & Y_d(\Delta\phi_i + \Delta\Gamma_i K)\\ 0 & M_2(\phi_{di} + \Gamma_{di}K)\end{bmatrix} & \\ \begin{bmatrix} M_1 - Y_d & Y_d(\Delta\phi_i + \Delta\Gamma_i K)\\ 0 & M_2(\phi_{di} + \Gamma_{di}K)\end{bmatrix}^T & \\ M & \end{bmatrix} > 0, \quad i = 1, \ldots, 32 \quad (41)$$

$$M_o < \xi M \quad (42)$$

where $Y_d = M_1 L_d$.

$$M = \begin{bmatrix} M_1 & 0\\ 0 & M_2\end{bmatrix} \quad \text{and } M_0 = \begin{bmatrix} M_{01} & 0\\ 0 & M_{02}\end{bmatrix}$$

are diagonal matrices. The matrices M_1 and Y_d can be obtained by solving the following optimization problem:

$$\begin{aligned} &\min\ \xi \quad M_o,\ M > 0\\ &\textit{subject to}\ (41)\ \textit{and}\ (42)\end{aligned} \quad (43)$$

where ξ denotes the decay rate of the tracking error (40). (43) means that M_o, M are chosen so that ξ is minimized while satisfying (41) and (42). The minimum ξ will yield the fastest convergence for the calculated errors.

As a result, the robust optimal disturbance observer gain can be determined as $L_d = M_1^{-1} Y_d$.

IV. PROPOSED CONTROL DESIGN

A. DESIRED STEADY-STATE CONDITION

It is assumed that with $L_g = 0$, the states and control input in steady-state can be obtained from (34) following the reference currents i_2^{qo} and i_2^{do}

$$v_c^{qo} = (R_2)_n i_2^{qo} + (L_2)_n \omega i_2^{do} + e^{qo} - \frac{(L_2)_n}{T_s} d_L^o(1) \quad (44)$$

$$v_c^{do} = -(L_2)_n \omega i_2^{qo} + (R_2)_n i_2^{do} + e^{do} - \frac{(L_2)_n}{T_s} d_L^o(2) \quad (45)$$

$$i_1^{qo} = i_2^{qo} + (C_f)_n \omega v_c^{do} - \frac{(C_f)_n}{T_s} d_L^o(5) \quad (46)$$

$$i_1^{do} = i_2^{do} - \left(C_f\right)_n \omega v_c^{qo} - \frac{\left(C_f\right)_n}{T_s} d_L^o \,(6)\,. \tag{47}$$

Moreover, the steady-state control input values can be determined as

$$u^{qo} = (R_1)_n\, i_1^{qo} + (L_1)_n\, \omega i_1^{do} + v_c^{qo} - \frac{(L_1)_n}{T_s} d_L^o \,(3) \tag{48}$$

$$u^{do} = -(L_1)_n\, \omega i_1^{qo} + (R_1)_n\, i_1^{do} + v_c^{do} - \frac{(L_1)_n}{T_s} d_L^o \,(4)\,. \tag{49}$$

To implement the steady-state values from (44) – (49), e^o and d_L^o are replaced by the grid voltage estimation $\hat{e}\,(k)$ and lumped disturbance observer $\hat{d}_L\,(k)$.

B. ROBUST CONTROLLER GAIN DESIGN

It is assumed here that the control input is designed as follows:

$$u\,(k) = K\tilde{e}_x\,(k) + u^0, \tag{50}$$

A cost function can be established based on the dynamic state error and control input, as follows:

$$J\,(k) = \tilde{e}_x\,(k+1)^T P \tilde{e}_x\,(k+1) + \delta u(k)^T R \delta u(k) \tag{51}$$

where P is a diagonal matrix and R is symmetric.

To ensure the stability of the system, the weighting matrices P and R and the controller gain K must be determined such that the cost function $J(k)$ monotonically decreases; i.e.,

$$\begin{aligned} &J\,(k) - J\,(k-1) < 0 \\ \Longleftrightarrow\ &\tilde{e}_x^T\,(k)\left[(\phi_d + \Gamma_d K)^T P\,(\phi_d + \Gamma_d K) + K^T R K - P\right] \\ &\quad \times \tilde{e}_x\,(k) - \tilde{e}_x^T\,(k-1)\, K^T R K \tilde{e}_x\,(k-1) < 0, \quad \forall k. \end{aligned} \tag{52}$$

It can be seen that the second term on the right-hand side of (52) is negative definite. To satisfy the condition of (52), the conditions of the first term should be satisfied:

$$P - (\phi_d + \Gamma_d K)^T P\,(\phi_d + \Gamma_d K) - K^T R K > 0. \tag{53}$$

The convergence rate ξ can be inserted into (53) as follows:

$$P - (\phi_d + \Gamma_d K)^T P\,(\phi_d + \Gamma_d K) - K^T R K > \left(1 - \xi^2\right) P \tag{54}$$

with $0 < \xi < 1$. Let $P_o = \xi^2 P$, and (54) can be rewritten as

$$P_o - (\phi_d + \Gamma_d K)^T P\,(\phi_d + \Gamma_d K) - K^T R K > 0. \tag{55}$$

Let $Q_o^{-1} = P_o$, $Q^{-1} = P$. By multiplying Q_o on the left- and right-hand sides of each term of (55), we have

$$Q_o - (\phi_d Q_o + \Gamma_d Y_k)^T Q^{-1} (\phi_d Q_o + \Gamma_d Y_k) - Y_k^T R Y_k > 0 \tag{56}$$

where $Y_k = K Q_o$. Applying the Schur complement, (56) can be rewritten as

$$\begin{bmatrix} Q_o & Y_k^T & (\phi_d Q_o + \Gamma_d Y_k)^T \\ Y_k & R^{-1} & 0_{2x6} \\ \phi_d Q_o + \Gamma_d Y_k & 0_{6x2} & Q \end{bmatrix} > 0. \tag{57}$$

Because the system is affected by the model uncertainties, we propose that all possibilities of (Φ_{di}, Γ_{di}) should be considered, i.e., $(\Phi_{di}, \Gamma_{di})\,, i = 1, \ldots, p$, in (57). To this end, we consider the revised system model of

$$\begin{bmatrix} Q_o & Y_k^T & (\phi_{di} Q_o + \Gamma_{di} Y_k)^T \\ Y_k & R^{-1} & 0_{2x6} \\ \phi_{di} Q_o + \Gamma_{di} Y_k & 0_{6x2} & Q \end{bmatrix} > 0. \tag{58}$$

To minimize the control input with regard to the selected convergence rate ξ, the robust controller gain K with the presence of uncertainties can be obtained by solving the LMIs optimization problem as

$$\begin{aligned} &\min\ -trace(Q_o) \quad \text{subject to (58)} \\ &Q, Q_o > 0 \end{aligned} \tag{59}$$

As long as Q_0 and Y_k are determined using the SeDuMi toolbox [18], the robust controller gain can then be computed as

$$K = Y_k Q_0^{-1}. \tag{60}$$

Consequently, the cost function (51) monotonically decreases; thus, a robust controller gain K guarantees the stability of the system.

The design process of the proposed control method can be summarized as follows.

Step 1: Derive the discretized model (14)-(18).

Step 2: Solve (27) to obtain L_z with initial values of $\mu_x = 1$. Increase μ_x if the observer performance is not robust to changes in the LCL parameter uncertainties and the grid impedance.

Step 3: Solve (43) and (59) to obtain the lumped disturbance L_d, and controller gains K with an initial value of $\mu_k = 1$, Increase μ_k if the system performance is not robust to changes in the LCL parameter uncertainties and the grid impedance.

V. FREQUENCY RESPONSE ANALYSIS

In the previous section, all of the observer and controller gains were obtained separately. This section presents the entire closed-loop system frequency response to demonstrate reference tracking and disturbance rejection.

TABLE 1. Parameters of the three-phase Inverter.

Symbol	Description	Value
DC	DC voltage	105 V
e^{abc}	Phase grid voltage	40 V
F_s	Grid voltage frequency	60 Hz
T_s	Sampling time	100 μs
$(R_1)_n/(R_2)_n$	Filter resistance	0.1/0.14 Ω
$(L_1)_n/(L_2)_n$	Filter inductance	1.4/0.7 mH
$\left(C_f\right)_n$	Filter capacitor	5.0 μF

Inserting $\hat{x}(k+1)$ from (28) into (32) will yield the following:

$$\hat{d}_L\,(k+1) = \hat{d}_L\,(k) + L_d L_x \left(y\,(k) - \hat{y}\,(k)\right) \tag{61}$$

The entire system can be established by combining the dynamics system (11), the observer dynamics (17), (28), and (61) using the control input (50).

$$\begin{cases} x(k+1) = \phi_n x(k) + \Gamma_n u(k-1) + H_n e(k) + d_L(k) \\ \hat{x}(k+1) = \phi_n \hat{x}(k) + \Gamma_n u(k-1) + H_n \hat{e}(k) \\ \qquad + L_x \left(y(k) - C_d \hat{x}(k) \right) + \hat{d}_L(k) \\ \hat{e}(k+1) = \hat{e}(k) + L_e \left(y(k) - C_d \hat{x}(k) \right) \\ \hat{d}_L(k+1) = \hat{d}_L(k) + L_d L_x \left(y(k) - C_d \hat{x}(k) \right) \end{cases} \tag{62}$$

The overall system (62) can be represented as block diagram as shown in Fig. 3.

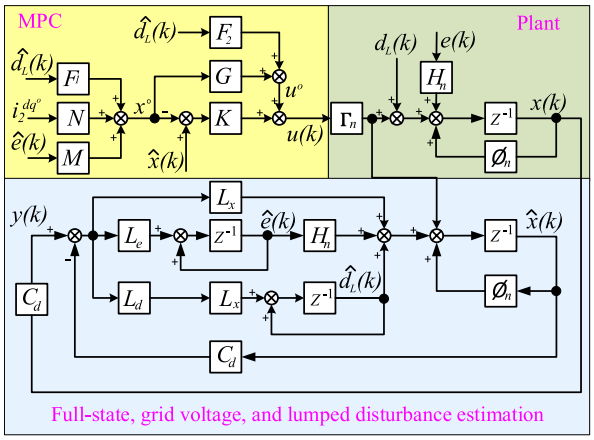

FIGURE 3. Detailed block diagram of the proposed MPC controller along with the full-state and disturbance observer.

The steady-state values in (44)-(49) can be rewritten as

$$x^o = Nr + M\hat{e} + F_1 \hat{d}_L \tag{63}$$

and

$$u^o = Gx^o + F_2 \hat{d}_L \tag{64}$$

where

$$N = \begin{bmatrix} 1 & 0 \\ 0 & 1 \\ 1 - C_f\omega^2 L_2 & C_f\omega R_2 \\ -C_f\omega R_2 & 1 - C_f\omega^2 L_2 \\ R_2 & L_2\omega \\ -L_2\omega & R_2 \end{bmatrix}, \quad M = \begin{bmatrix} 0 & 0 \\ 0 & 0 \\ 0 & C_f\omega \\ -C_f\omega & 0 \\ 1 & 0 \\ 0 & 1 \end{bmatrix},$$

$$F_1 = \begin{bmatrix} 0 & 0 & 0 & 0 & 0 & 0 \\ 0 & 0 & 0 & 0 & 0 & 0 \\ 0 & -C_f\omega L_2/T_s & 0 & 0 & -C_f/T_s & 0 \\ C_f\omega L_2/T_s & 0 & 0 & 0 & 0 & -C_f/T_s \\ -L_2/T_s & 0 & 0 & 0 & 0 & 0 \\ 0 & -L_2/T_s & 0 & 0 & 0 & 0 \end{bmatrix},$$

$$G = \begin{bmatrix} 0 & 0 & R_1 & L_1\omega & 1 & 0 \\ 0 & 0 & -L_1\omega & R_1 & 0 & 1 \end{bmatrix}, \quad \text{and}$$

$$F_2 = \begin{bmatrix} 0 & 0 & -L_1/T_s & 0 & 0 & 0 \\ 0 & 0 & 0 & -L_1/T_s & 0 & 0 \end{bmatrix}.$$

We consider the open-loop and closed-loop frequency responses to verify the effect of the proposed control scheme in the frequency domain. The closed-loop system is obtained by inserting (50), (63), and (64) into (62). The open-loop system is obtained from the closed-loop system in which the feedback loops from $\hat{x}(k)$ and $\hat{e}(k)$ are disconnected. Then, the closed-loop and open-loop systems can be expressed correspondingly as

$$x_{k+1}^{cl} = \phi_{cl} x_k^{cl} + \Gamma_{cl} u_{cl} \tag{65}$$

$$y_k^{cl} = C_{cl} x_k^{cl} \tag{66}$$

and

$$x_{k+1}^{ol} = \phi_{ol} x_k^{ol} + \Gamma_{ol} u_{ol} \tag{67}$$

$$y_k^{ol} = C_{ol} x_k^{ol} \tag{68}$$

where

$$x_k^{cl} = x_k^{ol} = \begin{bmatrix} x(k) & \hat{x}(k) & \hat{e}(k) & \hat{d}_L(k) \end{bmatrix}^T,$$

$$u_{cl} = u_{ol} = \begin{bmatrix} r(k) & e(k) & d_l(k) \end{bmatrix}^T,$$

$$\Gamma_{cl} = \Gamma_{ol} = \begin{bmatrix} \Gamma_n(GN - KN) & H_n & I_{6x6} \\ \Gamma_n(GN - KN) & 0_{6x2} & 0_{6x6} \\ 0_{2x2} & 0_{2x2} & 0_{2x6} \\ 0_{6x2} & 0_{6x2} & 0_{6x6} \end{bmatrix},$$

$$\phi_{cl} = \begin{bmatrix} \phi_n & \Gamma_n K \\ L_x C_d & \phi_n + \Gamma_n K - L_x C_d \\ L_e C_d & -L_e C_d \\ L_d L_x C_d & -L_d L_x C_d \end{bmatrix}$$
$$\begin{bmatrix} \Gamma_n(GM - KM) & \Gamma_n(GF_1 + F_2 - KF_1) \\ \Gamma_n(GM - KM) + H_n & \Gamma_n(GF_1 + F_2 - KF_1) + I_{6x6} \\ I_{2x2} & 0_{2x6} \\ 0_{6x2} & I_{6x6} \end{bmatrix}$$

$$\phi_{ol} = \begin{bmatrix} \phi_n & 0_{6x6} \\ L_x C_d & \phi_n - L_x C_d \\ L_e C_d & -L_e C_d \\ L_d L_x C_d & -L_d L_x C_d \end{bmatrix}$$
$$\begin{bmatrix} 0_{6x2} & \Gamma_n(GF_1 + F_2 - KF_1) \\ 0_{6x2} & \Gamma_n(GF_1 + F_2 - KF_1) + I_{6x6} \\ I_{2x2} & 0_{2x6} \\ 0_{6x2} & I_{6x6} \end{bmatrix}$$

The transfer function in the z-domain of the closed-loop and open-loop systems can be expressed as follows:

$$G_{cl} = C_{cl}(zI - \phi_{cl})^{-1} \Gamma_{cl} \tag{69}$$

and

$$G_{ol} = C_{ol}(zI - \phi_{ol})^{-1} \Gamma_{ol} \tag{70}$$

Note that the transfer function in (69) and (70) describe the transfer function from $r = \begin{bmatrix} i_2^{qo} & i_2^{do} \end{bmatrix}^T$ to $y(k)$ (reference tracking) and $e = \begin{bmatrix} e^q & e^d \end{bmatrix}^T$ to $y(k)$ (disturbance rejection). Fig. 4a shows the reference tracking of the open-loop and closed-loop systems, respectively. It can be seen that the uncertain parameter $L_1 = 2.3\ mH$ (increasing 165%) and the presence of grid impedance $L_g = 4.15\ mH$ are adequately offset, with zero phases and gain nearly at unity in terms of

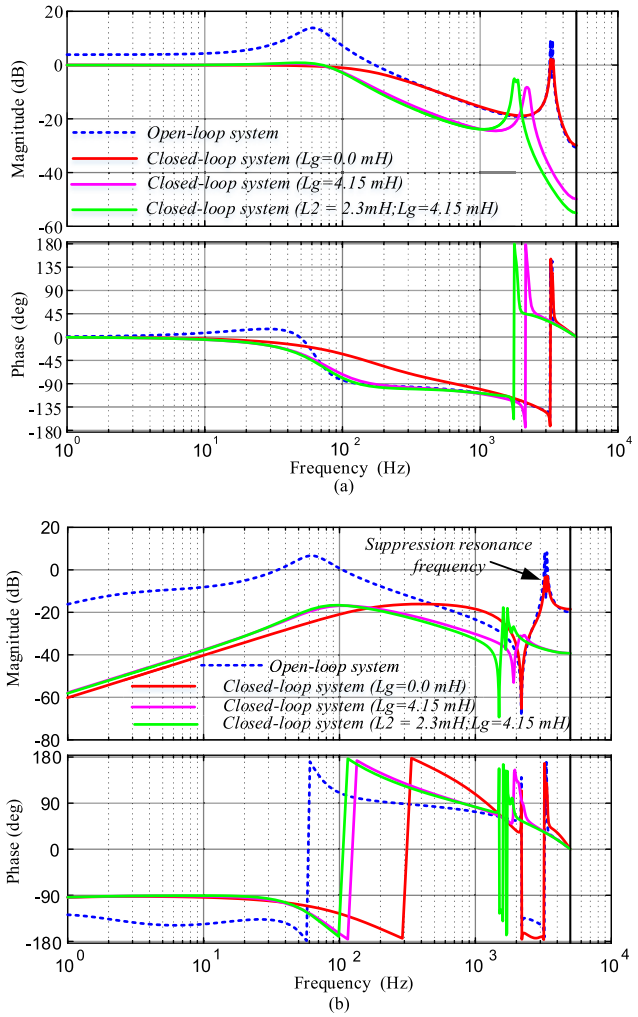

FIGURE 4. Frequency responses of the open-loop and closed-loop systems with SCR = 3.67. (a) Control to output responses from $r(k)$ to $y(k)$. (b) Disturbance rejection response from $e(k)$ to $y(k)$.

the magnitude leading to excellent tracking performance at the fundamental frequency.

The frequency responses of the grid voltage to the output system are presented in Fig. 4b to verify the disturbance rejection. This figure indicates that the magnitude of the open-loop system is greater than zero at the LCL resonance; however, the magnitude of the closed-loop system is less than zero in all frequency ranges. It can be concluded that the proposed control scheme effectively eliminates the disturbance rejection issue.

To further investigate the stability analysis of the overall system against with the variation of the parameter uncertainties, eigenvalues of the error dynamics are exhibits as follows. First, the error dynamics of the full-state and grid voltage observer (19) and the lumped disturbance observer (40) are augmented as:

$$\begin{bmatrix} e_z(k+1) \\ e_d(k+1) \end{bmatrix} = \begin{bmatrix} \phi_z - L_z C_z & 0_{12\times 8} \\ 0_{8\times 12} & \psi \end{bmatrix} \begin{bmatrix} e_z(k) \\ e_d(k) \end{bmatrix} \quad (71)$$

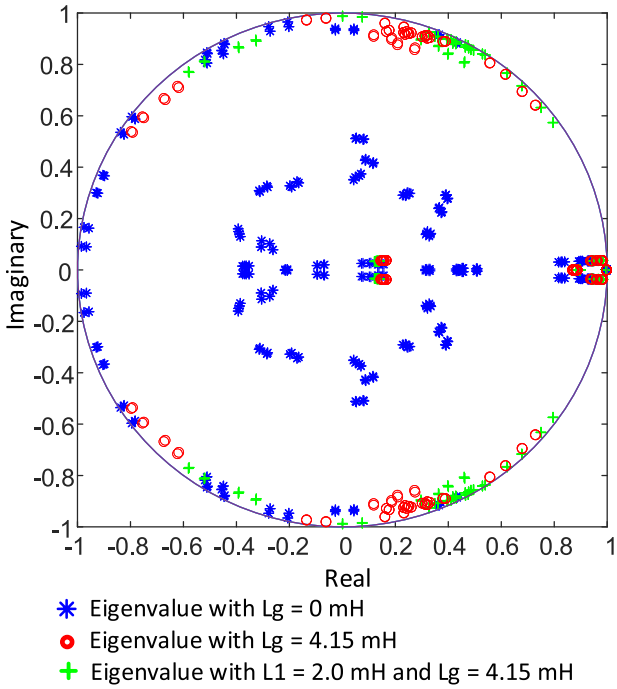

FIGURE 5. Eigenvalues of the entire error dynamics system under proposed observer and controller.

By checking the eigenvalues of this overall error dynamics (71) under grid impedance variations, we can conclude that the overall system is stable with the grid impedance less than $L_g = 4.15$ mH.

The eigenvalues of the entire error dynamics system are shown in Fig.5. It can be observed that all the eigenvalues stay inside the boundary of the unit circle under the grid impedance variation ($L_g = 0.0\ mH$, $L_g = 4.15\ mH$, and $L_1 = 2.0\ mH$, $L_g = 4.15\,mH$), which indicates that the entire system is stable.

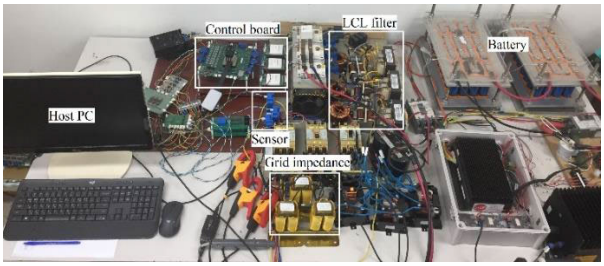

FIGURE 6. Experimental setup.

VI. SIMULATION AND EXPERIMENTAL RESULTS

In this section, simulation and experiment results are presented to demonstrate the effectiveness of the proposed control scheme. Fig.6 shows the experimental setup, consisting of a voltage source (batteries - LIFePO4 - 105V), a three-phase LCL filter, current sensors, and a DSP TMS320F28377 device. In order to meet the DC voltage of battery pack, an isolation transformer is used to lower the grid voltage to 40 V. Fluke434 power quality analysis

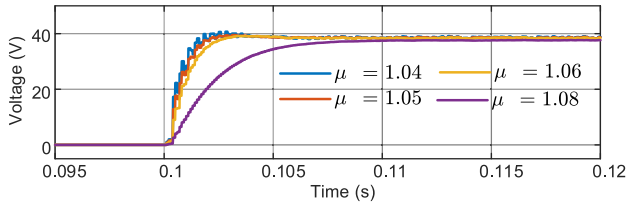

FIGURE 7. Simulation results regarding tuning the grid voltage observer using various of μ.

and Multi-Can analyzer devices were employed to save the experimental results.

A. TUNING FOR CURENT CONTROL

The best values of μ are obtained as follows:

In Fig.7, the grid voltage estimation versus different values of μ is presented. The figure indicates that as the values of μ decreases from 1.08 to 1.04, the better voltage estimation performance is achieved. However, when the μ is lesser than 1.04, overshoot increases as the values of μ reduce further. Based on this observation, the observer gain L_z with $\mu = 1.06$ is selected for the best performance.

Similarly, the proposed controller gain K and lumped disturbance observer gain L_d are found by tuning μ. Fig.8 shows the grid-side current along the d-axis and q-axis for different values of μ when the grid impedance changes at $t = 0.2$ s. It can be observed that the controller and lumped disturbance observer gains with $\mu = 3.0$ exhibit a better performance than that with other μ.

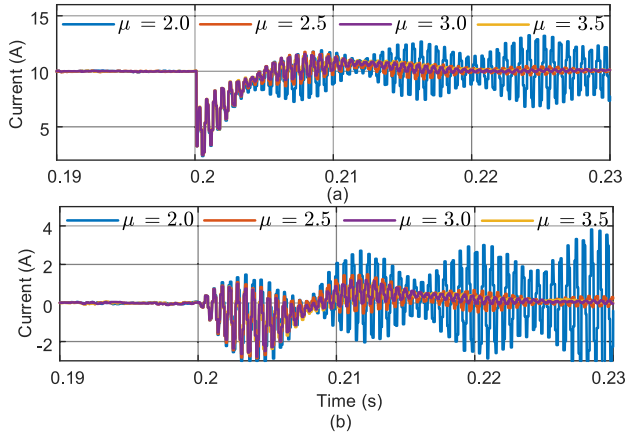

FIGURE 8. Simulation results regarding tuning performance of the current controller using various of μ considering a grid impedance change from 0 to 4.15 mH at $t = 0.2$ s. (a) Grid current along q-axis. (b) Grid current along the d-axis.

B. SIMULATION RESULTS

To highlight the efficacy of the proposed control scheme, a proportional-integral controller (PI) [19] and an MPC developed [14] in earlier work are compared to the proposed control method. For a fair comparison, the PI controller gains are tuned according to symmetrical optimum in the former study [19], and feedforward terms are added to the controller. The PI gains are set to $K_p = 1.25$ and $K_i = 252$.

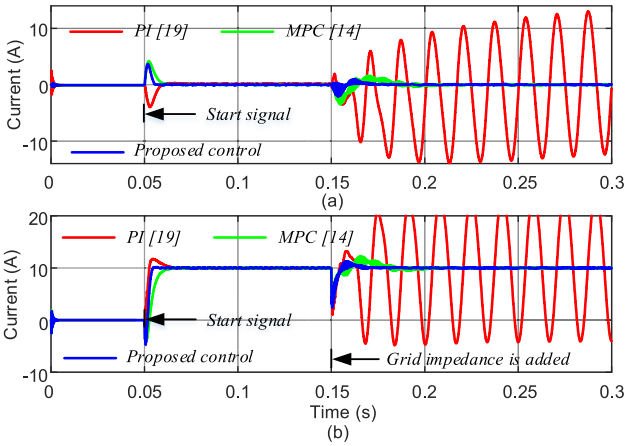

FIGURE 9. Simulation results for current control with and without grid impedance ($L_g = 4.15$ *mH*): (a) Grid-side current along the q-axis, and (b) Grid-side current along the d-axis.

Fig. 9 shows the grid-side current along the dq-axis during the start-up process with and without the presence of grid impedance. The system works with nominal values from $t = 0.05$ s to $t = 0.15$ s, and the system operates with $L_g = 4.15$ mH from $t = 0.15$ s to $t = 0.3$ s. It can be seen that all controllers work well with the conditions of the nominal parameters. However, the proposed robust control scheme exhibits the fastest transient response along the d-axis and the lowest overshoot along the q-axis among the three controllers. Moreover, when grid impedance is added at $t = 0.15$ s, the PI controller undergoes larger oscillation. This also causes grid-current oscillation of the MPC and the proposed control scheme; however, the proposed control method exhibits less oscillation compared to the MPC case under grid impedance, as shown in Figs. 9a and 9b.

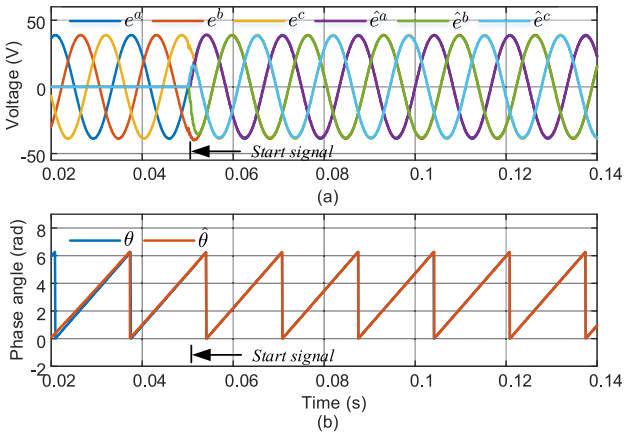

FIGURE 10. Simulation results. (a) The measured and estimated grid voltage. (b) The measured and estimated grid phase angle.

To verify the optimal observer gain, the measured and estimated grid voltages are shown in Fig. 10a. This clearly shows that the estimated grid voltage immediately converges to the actual voltage. Similarly, the estimated grid phase angle tracks the actual value, as shown in Fig. 10b. It should be

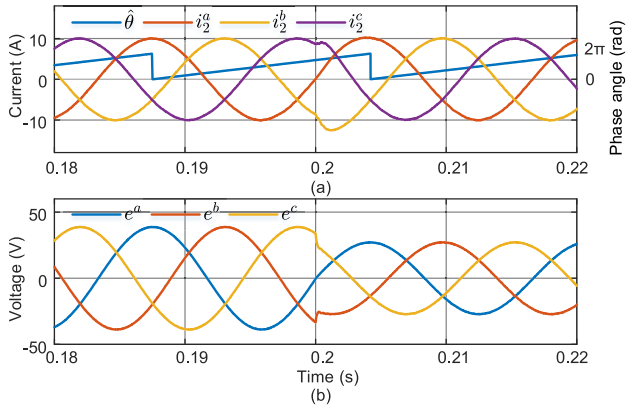

FIGURE 11. Simulation results of proposed control scheme under grid voltage variation. (a) Grid-side current and grid phase angle. (a) Grid voltage sudden drop of 30% the magnitude.

noted that the initial grid phase angle is detected before the system starts using grid current sensors.

Fig.11 shows the grid-side current and grid phase angle under the grid voltage dip of 30% on three-phase at $t = 0.2$ s. It can be seen that a sudden drop in the magnitude of the grid voltage, as shown in Fig.11a causes a slight oscillation on the grid-side current, and it take about 0.003 s for the grid-side current to converge to the steady-state values. In addition, the sudden change of the grid voltage does not affect the grid phase angle.

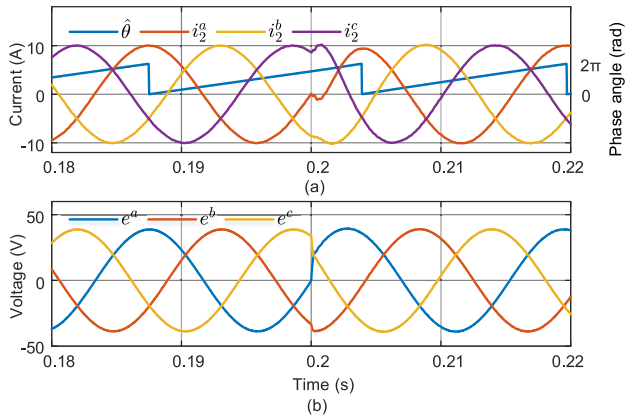

FIGURE 12. Simulation results of proposed control scheme under the rapid phase jump of 30° at $t = 0.2$ s. (a) Grid-side current and grid phase angle. (a) Grid voltage.

Fig.12 shows the performance of the grid-side current when the grid phase angle jumps rapidly by 30° at $t = 0.2$ s. It can be observed that the sudden change of the phase leads to a slight overshoot on the grid-side current as well as causes a slight oscillation on the grid voltage. However, they rapidly converge to the steady-state values after a short time. It can be concluded that the proposed control scheme can deal with the variations amplitude and the phase angle of the grid voltage.

C. EXPERIMENTAL RESULTS

For further verification of the proposed control scheme, experiments were carried out under conditions similar to those used in the simulations. It should be noted that a practical grid is used. It is difficult to change the grid impedance suddenly, and for this reason, the experiments will be verified in different conditions separately.

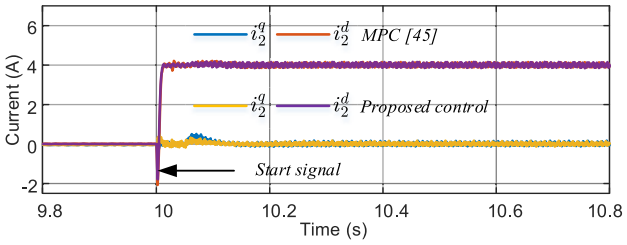

FIGURE 13. Experimental results for the grid current control along the dq-axis during the start-up at $t = 10$ s.

Fig. 13 shows the grid-side current along the dq-axis during start-up at $t = 10$ s without the presence of grid impedance. It can be seen that the MPC as developed in earlier work [14] and the proposed method are quite similar. Both control methods exhibit a rapid transient response without overshoot.

To demonstrate synchronization with the grid and verify the robust optimal observer gain, Fig. 14 shows the measured and estimated grid phase angle and grid voltage. It can be observed that the estimated grid phase angle and estimated grid voltage quickly converge to the actual values. The estimated grid phase angle immediately reaches the actual grid phase angle, as shown in Fig. 14(a). Likewise, the estimated grid voltage requires less than half of the number of cycles to converge to the actual voltage, as shown in Fig. 14(b).

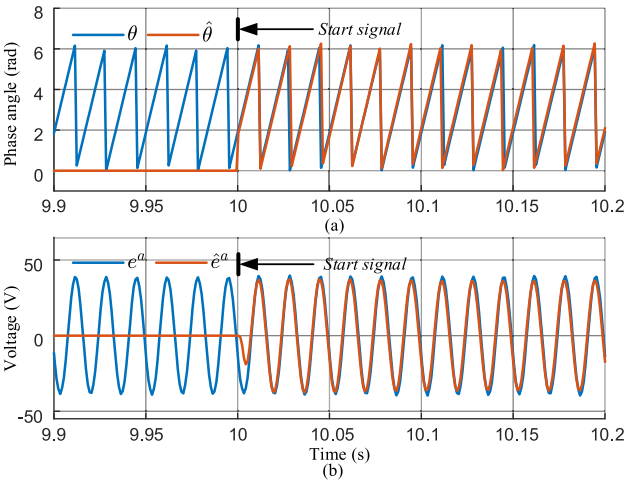

FIGURE 14. Experimental results for the measured and estimated grid phase angle (a) and the measured and estimated grid voltage (b).

To validate the robustness of the proposed control method to the presence of grid impedance, Fig.15 presents the experimental results for the grid-side current in the presence of grid impedance, with $L_g = 4.15$ mH. It can be seen that the MPC [14] and the proposed control scheme operate well under grid impedance at $t = 10$ s. However, the MPC [14] exhibits current overshoot on both the d-axis and q-axis, and it takes 0.3 s to converge to steady-state values. In contrast,

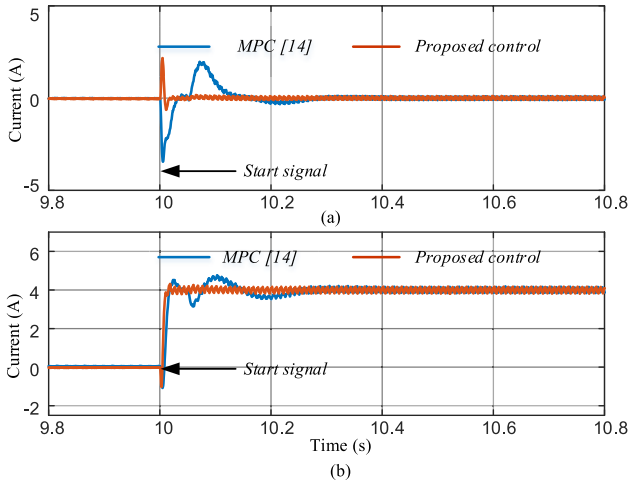

FIGURE 15. Experimental results for the current control during the start-up at $t = 10$ s with $L_g = 4.15$ mH. (a) Grid-side current along q-axis. (b) Grid-side current along d-axis.

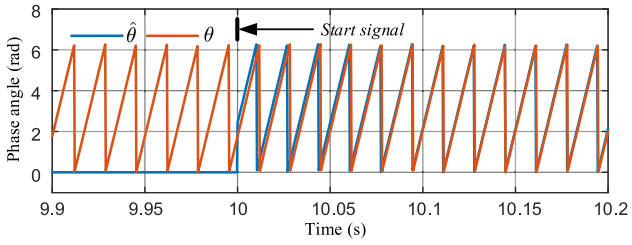

FIGURE 16. Experimental result for the measured and estimated grid phase angle with $L_g = 4.15$ mH.

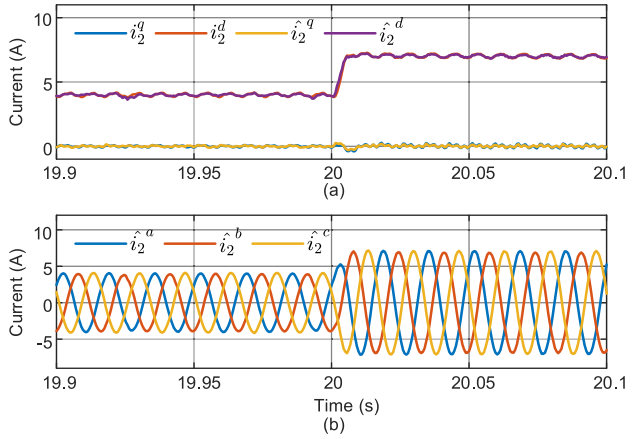

FIGURE 17. Experimental result for the grid-side current in a steady-state with $L_g = 4.15$ mH: (a) Measured and estimated grid-side current along the dq-axis, and (b) Estimated grid-side current in the waveform.

the proposed control method exhibits an excellent transient response. Fig. 8 indicates that the dq-axis undergoes minimal overshoot, taking 0.02 s to converge to steady-state values. Similarly, the estimated grid phase angle is well matched with the actual grid phase angle, even when grid impedance is added, as shown in Fig.16.

To examine whether the state observer is working well, Fig. 17 shows the estimated grid-side current on the dq-axis in the presence of grid impedance, indicating that the reference

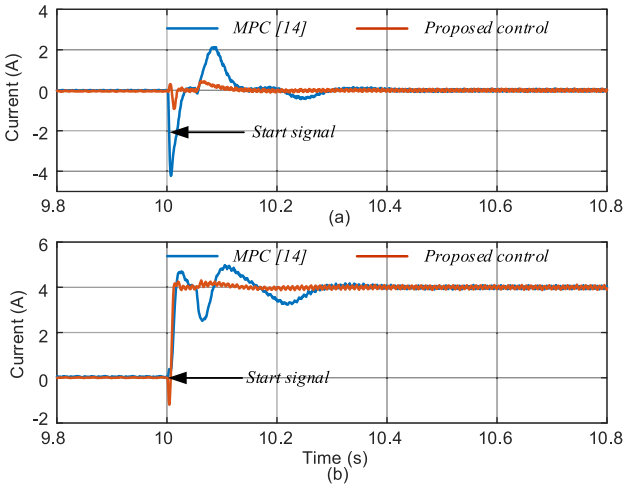

FIGURE 18. Experimental results for the grid-side current by the MPC developed in earlier work [14] and the proposed control scheme under LCL parameter uncertainties and the presence of grid impedance: (a) Grid current along the q-axis, and (b) Grid current along the d-axis.

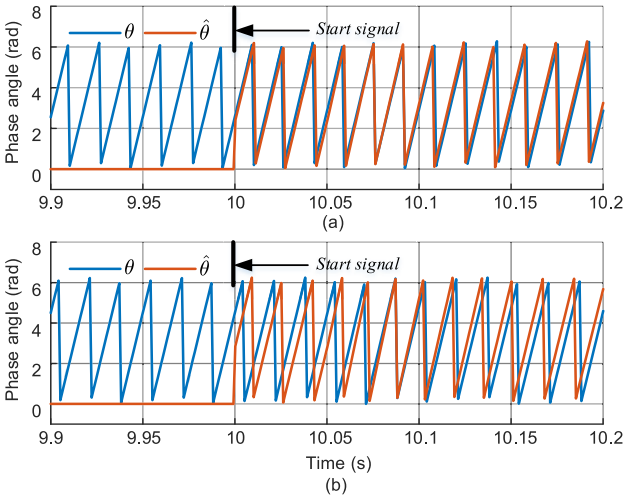

FIGURE 19. Experimental results for the measured and estimated grid phase angles by the MPC from the literature [14] and the proposed control scheme under LCL parameter uncertainties and in the presence of grid impedance: (a) Proposed control scheme, and (b) MPC [14].

currents change from 4 A to 7 A at $t = 20$ s. The figure shows that the estimated grid-side current coincides with the actual current values, as shown in Fig. 17(a). Moreover, the estimated grid-side current in the waveform is shown in Fig. 17(b).

To confirm the robustness of the proposed control scheme, the inductor L_1 and L_g are changed from nominal values ($L_1 = 1.4$ mH and $L_g = 0.0$ mH) to new values ($L_1 = 2.3$ mH, representing an increase of 165% compared to the nominal values and grid impedance $L_g = 4.15$ mH) at the beginning of the experiment. Fig. 18 shows the experimental results for the grid-side current along the dq-axis. It can be seen that the MPC [14] exhibits a transient overshoot response on both the d-axis and q-axis. It takes 0.4 s to return to steady-state values. For this reason, the estimated grid phase angle does not match the actual value upon a transient response, as shown in Fig. 19(b). On the other hand,

the proposed method exhibits a fast transient response with a slight overshoot and only takes 0.1 s to converge to the steady-state values, as shown in Fig. 18. The estimated grid phase angle is well matched with the actual values, as shown in Fig. 19(a). The estimated grid phase angle immediately converges to the actual values because the initial grid phase angle is detected before the system start-up process. It can be concluded that the proposed control scheme can handle parameter uncertainties and grid impedance variations.

VII. CONCLUSION

This paper has presented a disturbance observer-based robust model predictive control scheme for a grid-voltage sensorless inverter that works without grid voltage measurements. It was demonstrated that the proposed control scheme could estimate not only the grid voltage but also the lumped disturbance to eliminate steady-state errors in the inverter system. Using the grid-side current sensor, the grid phase angle is detected before the system starts; thus, the transient response of the system is improved. A frequency response analysis proved that complete system stability, reference tracking, and disturbance rejection are achieved. Simulation and experimental results demonstrated the validity and effectiveness of the proposed control scheme. Additionally, the efficacy of the proposed method as demonstrated in the simulation and experimental results was compared with a similar strategy recently proposed in the literature [14] and with the conventional PI method [19].

REFERENCES

[1] J. Liang, H. Wang, and Z. Yan, "Grid voltage sensorless model-based predictive power control of PWM rectifiers based on sliding mode virtual flux observer," *IEEE Access*, vol. 7, pp. 24007–24016, 2019, doi: 10.1109/ACCESS.2019.2898687.

[2] S. Bayhan, "Grid voltage sensorless model predictive control for a single-phase T-type rectifier with an active power decoupling circuit," *IEEE Access*, vol. 9, pp. 19161–19174, 2021, doi: 10.1109/ACCESS.2021.3054773.

[3] X. Xiao, Y. Wu, J. Su, Y. Zhang, and J. Zhou, "An improved precise power control of voltage sensorless-MPC for PWM rectifiers," *IEEE Access*, vol. 8, pp. 220058–220068, 2020, doi: 10.1109/ACCESS.2020.3041526.

[4] H. Yang, Y. Zhang, J. Liang, J. Gao, P. Walker, and N. Zhang, "Sliding-mode observer based voltage-sensorless model predictive power control of PWM rectifier under unbalanced grid conditions," *IEEE Trans. Ind. Electron.*, vol. 65, no. 7, pp. 5550–5560, Jul. 2018, doi: 10.1109/TIE.2017.2774730.

[5] K. Jalili and S. Bernet, "Design of *LCL* filters of active-front-end two-level voltage-source converters," *IEEE Trans. Ind. Electron.*, vol. 56, no. 5, pp. 1674–1689, May 2009, doi: 10.1109/TIE.2008.2011251.

[6] A. Rahoui, A. Bechouche, H. Seddiki, and D. O. Abdeslam, "Grid voltages estimation for three-phase PWM rectifiers control without AC voltage sensors," *IEEE Trans. Power Electron.*, vol. 33, no. 1, pp. 859–875, Jan. 2018, doi: 10.1109/TPEL.2017.2669146.

[7] T. V. Tran and K.-H. Kim, "Frequency adaptive grid voltage sensorless control of LCL-filtered inverter based on extended model observer," *IEEE Trans. Ind. Electron.*, vol. 67, no. 9, pp. 7560–7573, Sep. 2020, doi: 10.1109/TIE.2019.2944075.

[8] R. A. Fantino, C. A. Busada, and J. A. Solsona, "Observer-based grid-voltage sensorless synchronization and control of a VSI-LCL tied to an unbalanced grid," *IEEE Trans. Ind. Electron.*, vol. 66, no. 7, pp. 4972–4981, Jul. 2019, doi: 10.1109/TIE.2018.2868255.

[9] K. H. Ahmed, A. M. Massoud, S. J. Finney, and B. W. Williams, "A modified stationary reference frame-based predictive current control with zero steady-state error for LCL coupled inverter-based distributed generation systems," *IEEE Trans. Ind. Electron.*, vol. 58, no. 4, pp. 1359–1370, Apr. 2011, doi: 10.1109/TIE.2010.2050414.

[10] J. Kukkola and M. Hinkkanen, "State observer for grid-voltage sensorless control of a converter under unbalanced conditions," *IEEE Trans. Ind. Appl.*, vol. 54, no. 1, pp. 286–297, Jan./Feb. 2018, doi: 10.1109/TIA.2017.2749305.

[11] Y. A.-R. I. Mohamed, E. F. El-Saadany, and M. M. A. Salama, "Adaptive grid-voltage sensorless control scheme for inverter-based distributed generation," *IEEE Trans. Energy Convers.*, vol. 24, no. 3, pp. 683–694, Sep. 2009, doi: 10.1109/TEC.2008.2001448.

[12] Y. A.-R. I. Mohamed and E. F. El-Saadany, "A robust natural-frame-based interfacing scheme for grid-connected distributed generation inverters," *IEEE Trans. Energy Convers.*, vol. 26, no. 3, pp. 728–736, Sep. 2011, doi: 10.1109/TEC.2011.2141135.

[13] N. B. Lai, K.-H. Kim, and P. Rodriguez, "Voltage sensorless control scheme based on extended-state estimator for a grid-connected inverter," *IEEE Trans. Power Electron.*, vol. 35, no. 6, pp. 5873–5882, Jun. 2020, doi: 10.1109/TPEL.2019.2952898.

[14] N. N. N. Nam, N.-D. Nguyen, C. Yoon, M. Choi, and Y. I. Lee, "Voltage sensorless model predictive control for a grid-connected inverter with LCL filter," *IEEE Trans. Ind. Electron.*, early access, Jan. 14, 2021, doi: 10.1109/TIE.2021.3050395.

[15] B. Wang, Y. Xu, Z. Shen, J. Zou, C. Li, and H. Liu, "Current control of grid-connected inverter with LCL filter based on extended-state observer estimations using single sensor and achieving improved robust observation dynamics," *IEEE Trans. Ind. Electron.*, vol. 64, no. 7, pp. 5428–5439, Jul. 2017, doi: 10.1109/TIE.2017.2674600.

[16] N. N. Nam, M. Choi, and Y. I. Lee, "Model predictive control of a grid-connected inverter with LCL filter using robust disturbance observer," *IFAC-PapersOnLine*, vol. 52, no. 4, pp. 135–140, 2019, doi: 10.1016/j.ifacol.2019.08.168.

[17] J. S. Lim, C. Park, J. Han, and Y. I. Lee, "Robust tracking control of a three-phase DC-AC inverter for UPS applications," *IEEE Trans. Ind. Electron.*, vol. 61, no. 8, pp. 4142–4151, Aug. 2014, doi: 10.1109/TIE.2013.2284155.

[18] J. F. Sturm, "Using SeDuMi 1.02, a MATLAB toolbox for optimization over symmetric cones," *Optim. Methods Softw.*, vol. 11, nos. 1–4, pp. 625–653, 1999.

[19] J. Dannehl, F. W. Fuchs, S. Hansen, and P. B. Thøgersen, "Investigation of active damping approaches for PI-based current control of grid-connected pulse width modulation converters with LCL filters," *IEEE Trans. Ind. Appl.*, vol. 46, no. 4, pp. 1509–1517, Jul./Aug. 2010, doi: 10.1109/TIA.2010.2049974.

[20] S. Golestan, M. Monfared, F. D. Freijedo, and J. M. Guerrero, "Dynamics assessment of advanced single-phase PLL structures," *IEEE Trans. Ind. Electron.*, vol. 60, no. 6, pp. 2167–2177, Jun. 2013, doi: 10.1109/TIE.2012.2193863.

[21] M. Liserre, F. Blaabjerg, and S. Hansen, "Design and control of an LCL-filter-based three-phase active rectifier," *IEEE Trans. Ind. Appl.*, vol. 41, no. 5, pp. 1281–1291, Sep./Oct. 2005, doi: 10.1109/TIA.2005.853373.

[22] Y. Zhang, Z. Wang, J. Jiao, and J. Liu, "Grid-voltage sensorless model predictive control of three-phase PWM rectifier under unbalanced and distorted grid voltages," *IEEE Trans. Power Electron.*, vol. 35, no. 8, pp. 8663–8672, Aug. 2020, doi: 10.1109/TPEL.2019.2963206.

[23] T. V. Tran, K.-H. Kim, and J.-S. Lai, "Optimized active disturbance rejection control with resonant extended state observer for grid voltage sensorless LCL-filtered inverter," *IEEE Trans. Power Electron.*, vol. 36, no. 11, pp. 13317–13331, Nov. 2021, doi: 10.1109/TPEL.2021.3082938.

NGUYEN NGOC NAM was born in Phu Tho, Vietnam, in 1983. He received the B.S. degree in mechatronics engineering from Lac Hong University, Vietnam, in 2011, and the M.S. degree in mechatronics engineering from the Military Technical Academy, Vietnam, in 2015. He is currently pursuing the Ph.D. degree with the Department of Electrical and Information Engineering, Seoul National University of Science and Technology. His research interests include model predictive control, renewable energy, and power electronics.

NGOC-DUC NGUYEN received the B.Sc. degree in mechatronics from Ho Chi Minh City University of Technology, in 2014, and the M.S. and Ph.D. degrees in control engineering from Korea Maritime and Ocean University, South Korea, in 2016 and 2019, respectively.

He worked as a Postdoctoral Researcher with the Research Center for Electrical and Information Technology, Seoul National University of Science and Technology. His research interests include automatic control and its implementation on robotics, electrical machines, power converters, and hybrid battery.

CHANGWOO YOON received the B.S. and M.S. degrees in electrical engineering from Seoul National University of Science and Technology (SeoulTech), Seoul, South Korea, in 2007 and 2009, respectively, and the Ph.D. degree in energy technology program from Aalborg University, Aalborg, Denmark, in 2017. He was a Hardware Design Engineer with Advance Drive Technology, Anyang, South Korea, from 2009 to 2013. In 2015, he was a Visiting Scholar with the University of Manitoba, Canada. He was with Rolls-Royce@NTU Corporate Laboratory, Singapore, as a Research Fellow, from 2017 to 2018. He was a Senior Engineer with Xnergy Autonomous Power Technologies, Singapore, in 2019. Since 2020, he has been working as a Research Professor with the Research Center of Electrical and Information Technology (RCEIT), SeoulTech. His main research interest includes modeling and control of power electronics-based systems.

YOUNG IL LEE (Senior Member, IEEE) received the B.S., M.S., and Ph.D. degrees in control and instrumentation engineering from Seoul National University (SNU), in 1986, 1988, and 1994, respectively.

He was a Visiting Research Fellow with the Department of Engineering Science, Oxford University, from February 1998 to July 1999 and February 2007 to July 2007. He worked with Gyeongsang National University, from 1994 to 2001, and moved to Seoul National university of Science and Technology (SeoulTech), in 2001. He is currently a Professor with the Department of Electrical and Information Engineering, SeoulTech. His area of scientific interests include MPC for systems with input constraints and model uncertainties, MPC method for dc–dc, ac–dc converter and dc–ac inverter, control of EV chargers, control of AC motors for EV application, and energy management algorithm of micro-grids. He is also the Director of the Electrical Vehicle Society, Korea Institute of Electrical Engineering (KIEE), and the Research Center of Electrical and Information Technology, SeoulTech. He has been serving as an Editor for *International Journal of Control, Automation and Systems* (IJCAS), since 2017, and *International Journal of Automotive Technology* (IJAT), since 2019.